

Heating–freezing effects on the pore size distribution of a kaolinite clay

Zubin Darbari¹ · Karam A. Jaradat²  · Sherif L. Abdelaziz³ 

Received: 29 March 2017 / Accepted: 16 October 2017 / Published online: 24 October 2017
© Springer-Verlag GmbH Germany 2017

Abstract This study aims to quantify the effect of heating and freezing temperatures on the pore size distribution of saturated clays. Three kaolinite clay specimens were subjected to different temperatures: 20, 70, and -10 °C. Upon achieving the desired temperature for each specimen, the specimens were flash frozen in liquid nitrogen to preserve their microstructure. Each specimen was, then, freeze-dried for 24 h after which consecutive two-dimensional (2-D) SEM images were taken using a dual focused ion beam/scanning electron microscope. The produced 2-D images of each specimen were used to reconstruct three-dimensional tomographies of the specimens, which were analyzed to determine the pore size distribution at each temperature. Compared to the specimen at room temperature, the pores in the specimen subjected to -10 °C were larger; this is believed to be due to the formation of ice lenses inside the pores upon freezing and potential merging between initial pores to form larger pores. On the other hand, the heated specimen showed an increase in the volume of the smaller pores and a decrease in the volume of the larger pores compared to the specimen at room temperature. This opposite behavior between the small and large pores in the heated specimen is justified considering

(1) the easier flow of water out of the larger pores compared to that in the smaller pores and (2) the anisotropic nature of the thermal expansion of the clay particles.

Keywords Clay · Temperature · Kaolinite · Focused ion beam · Thermal cycle · Pore size distribution · Tomography · FIB/SEM

Introduction

Throughout the recent years, multiple studies have investigated the temperature effects on clay behavior under heating–cooling (Abuel-Naga et al. 2007; Baldi et al. 1988; Campanella and Mitchell 1968a; Cekerevac and Laloui 2004) and freezing–thawing cycles (Othman and Benson 1993; Tang and Yan 2015). These studies were motivated by different applications in which clays are subjected to extreme temperatures, either elevated or freezing, including the design of foundation elements rested on frozen soils, nuclear waste disposal barriers, clay liners for elevated temperature landfills (Rowe 2012), and recently thermo-active foundation systems (Abdelaziz and Ozudogru 2016; Knellwolf et al. 2011; Laloui et al. 2006). Therefore, a group of researchers focused on the behavior of fine-grained soils subjected to freezing and freeze–thaw cycles (Broms and Yao 1964; Chamberlain 1981; Chamberlain and Gow 1979; Eigenbrod 1996; Konrad 1987, 1989; Norrish and Rausell-Colom 1962; Qi et al. 2008). Meanwhile, another group considered the behavior of fine-grained soils at non-boiling/elevated temperatures and heating–cooling cycles, i.e., elevated temperatures followed by temperature recovery to the initial value (Abuel-Naga et al. 2005; Campanella 1965; Eriksson 1989; Hueckel and Baldi 1990; Hueckel et al. 2009;

✉ Sherif L. Abdelaziz
Sherif.abdelaziz@stonybrook.edu

¹ Department of Material Science and Engineering, Stony Brook University, 103 Heavy Engineering Bldg, Stony Brook, NY 11794-4424, USA

² Department of Civil Engineering, Stony Brook University, 103 Heavy Engineering Bldg, Stony Brook, NY 11794-4424, USA

³ Department of Civil Engineering, Stony Brook University, 2424 Computer Science Bldg, Stony Brook, NY 11794-4424, USA

Kuntiwattanakul et al. 1995; Laloui 2001; Mitchell 1969; Paaswell 1967; Plum and Esrig 1969; Sultan et al. 2002; Tanaka et al. 1997). These previous efforts led to significant improvements in understanding the behavior of soils at isothermal temperatures ranging from below-freezing to elevated temperatures. In fact, the results of soil tests conducted at various temperatures within this temperature range form logical thermal evolutions of various physical and mechanical soil properties including hydraulic conductivity, volumetric strains, preconsolidation pressure, and shear strength.

Considering heating and heating–cooling cycles, it is currently understood that fast (undrained) heating of clays increases the pore water pressure due to the difference in thermal expansions of the clay fabric and the pore water (Campanella and Mitchell 1968a). This thermally induced increase in the pore water pressure reduces the effective stress and, therefore, the shear strength of the clay (Hueckel et al. 2009). On the other hand, slow (drained) heating of clays causes thermally induced volume changes. These thermally induced volume changes were believed to depend on the stress history of the clay tested in the form of the overconsolidation ratio (Burghignoli et al. 2000; Donna and Laloui 2015). However, it was recently discussed that the thermally induced volumetric changes depend more on the sign of the recent change in the mean stress applied on the soil (Coccia and McCartney 2016a, b). While supported by experimental tests, understanding the thermally induced microfabric changes will provide a better explanation to justify these macroscale observations, and it will facilitate the development of more accurate thermomechanical constitutive relations.

Additionally, clays subjected to freezing undergo volumetric expansion with an increase in the permeability, yield stress, and the shear strength (Czurda and Hohmann 1997; Qi et al. 2006; Wang et al. 2007). On the other hand, thawing a frozen clay develops a net contractive strain (Eigenbrod 1996; Othman and Benson 1993) and a decrease in the shear strength (Broms and Yao 1964; Garham and Au 1985; Wang et al. 2007). While theoretical explanations for the microfabric alternations due to freeze–thaw exist (Konrad 1989), microscale experimental results supporting these theoretical explanations are absent.

Of particular interest to this study is the fact that the thermomechanical behavior of clays was always considered from only one side of the temperature path, i.e., either heating–cooling or freezing–thawing. We currently lack an understanding of the evolution of the clay behavior over the full temperature range from freezing to elevated temperatures. Therefore, robust constitutive relations predicting the response of clays over this full temperature range do not exist. Superimposing approximations from constitutive relations developed for heating–cooling to those

developed for freezing–thawing is believed to be inaccurate because of the nonlinearity of the clay behavior. Normally consolidated clays after freeze–thaw cycles, for instance, undergo an increase in the preconsolidation pressure (Qi et al. 2010), which is the same behavior observed after heating–cooling cycles (Plum and Esrig 1969). Moreover, contractive volumetric strains develop in normally consolidated clays after freeze–thaw cycles (Othman and Benson 1993) and, also, after heating–cooling cycles (Campanella and Mitchell 1968b). To explain these comparable clay responses under opposite temperature cycles, it is critical to start with understanding the effect of each temperature extreme on the clay microstructure. Then, the focus can be shifted toward considering the effects of complete freeze–heat cycles. This microstructure understanding will facilitate forming a comprehensive understanding of the thermomechanical behavior of cohesive soils generally and explicitly clays that, in turn, will allow developing more robust constitutive models.

In general, three main parameters are considered to explain the effects of temperature on clay microstructure; these parameters are the orientation of clay particles, pore size distribution, and pore connectivity. This paper focuses on understanding the temperature effects on the pore size distribution of a kaolinite clay by utilizing scanning electron microscope images to reconstruct the 3-D tomography of clay specimens subjected to different temperatures. The developed tomographies are, then, processed to approximate the pore size distributions corresponding to each temperature. Using the pore size distribution at the room temperature (20 °C) as a reference, the distributions developed at an elevated temperature (70 °C) and a freezing temperature (− 10 °C) are compared and, further, used to explain the macroscale volume changes for the respective temperatures.

Materials and samples preparation

The clay considered in this study is the Edgar Plastic Kaolin (EPK) from Edgar, FL. This clay has 100% of its particles finer than 25 μm as determined using sedimentation (hydrometer) analysis according to ASTM D7928-17 and presented in Fig. 1. Additionally, more than 96% of the minerals of the EPK clay were identified as kaolinite minerals using X-ray diffraction on the clay powder. EPK clay classifies as fat clay (CH), i.e., clay with high plasticity, according to the unified soil classification system (USCS) with plastic and liquid limits of 32 and 67%, respectively.

The considered samples were prepared by mixing the EPK clay powder with water and a dispersive agent at one-and-half times the clay liquid limit. The clay slurry was,

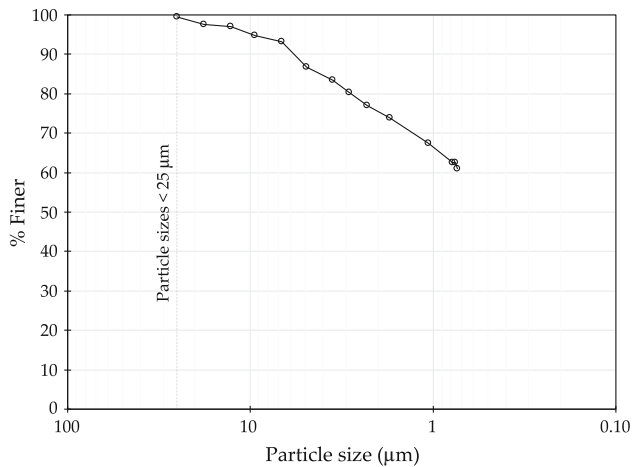


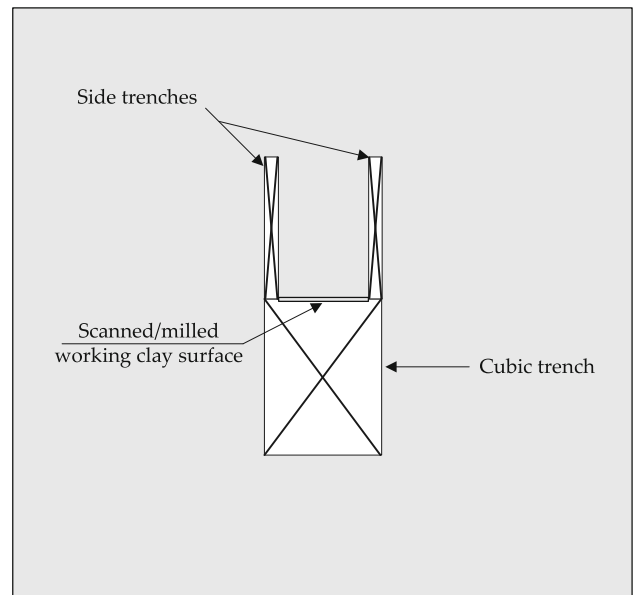
Fig. 1 Particle size distribution of the EPK kaolinite clay

then, subjected to one-dimensional (1-D) consolidation. In the end, small 1-mm cubical specimens were cut out of the bulk samples for the SEM/FIB work conducted in this study. The first specimen was maintained at the room temperature (20 °C), and it was used as a reference. The second specimen was subjected to 70 °C, while the third specimen was subjected to − 10 °C. Temperature changes for the second and the third specimens were applied by enclosing the specimens inside a freeze–thaw chamber at the desired temperature for 24 h. All specimens were immersed in liquid nitrogen for 20 min; then, they were freeze-dried for 24 h to preserve their microstructure (Mitchell and Soga 2005). The bottom and the top surfaces of each specimen were dry-polished using polishing papers with descending sizes; the smallest polishing paper size was 5 μm. The specimens were coated with silver coating on the sides and mounted on a SEM sample holder via a layer of silver paint. The top surfaces of the specimens were coated with a 20-nm layer of gold. Connectivity between the top gold coating and the silver coatings on the sides was ensured to minimize any charging effects during milling and imaging.

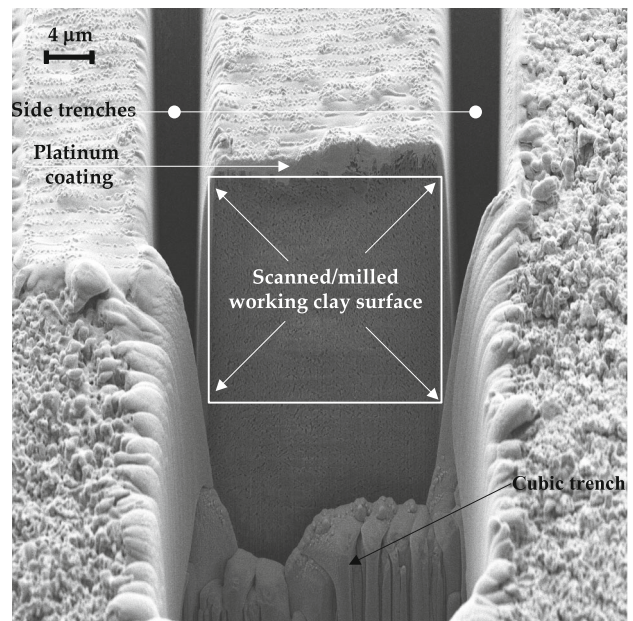
SEM/FIB imaging and milling

The SEM/FIB imaging was performed using a dual focused ion beam/scanning electron microscopy (FIB/SEM) at the Center of Functional Nanomaterials (CFN) at Brookhaven National Laboratory (BNL). Each specimen was placed at the eucentric height of the instrument (working distance = 4.2 mm), where the vertical electron beam and the inclined ion beam intersect. The procedure of milling and imaging started by milling a deep cube in the clay specimens using the maximum ion beam current of the instrument. The size of this cube was selected to be about twice

the size of the desired working surface. Since the used clay has 95% finer than 10 μm, the selected working surface area for milling and imaging was 20 × 20 × 20 μm, ensuring that most of the clay particles starting within the considered surface will also end within the imaged surfaces. After milling the large cubic, two side trenches were eroded as a guide for the milling/imaging process as shown in Fig. 2. The distance between these side trenches was about 12 μm, i.e., 2 μm more than the selected minimum



(a)



(b)

Fig. 2 Surface preparation for SEM/FIB work **a** schematic plan view of the milled cube and trenches and **b** SEM view of a prepared specimen

width of the desired working surface. Moreover, the extension of the trenches in the direction perpendicular to the working surface was at least 20 μm to ensure the continuity of the trenches along the desired specimen depth. Finally, a 50-nm platinum layer was deposited on the top surface of the specimens to reduce the curtaining effect due to the penetrating thickness of the ion beam during milling.

To optimize the milling/imaging process, preliminary milling attempts on sacrificial surfaces were conducted to select the milling settings (i.e., current and voltage) that will not melt clay particles while minimizing the milling/imaging time. For the used clay, it was found that a milling current of 20 pA with 30 kV voltage produced acceptable clay surfaces for imaging in 48–72 h. Therefore, these milling settings were used for the three considered specimens. After milling a surface, each milled surface was imaged using the electron beam set at a 86 nA current and 5 kV voltage. In the end, the ion beam was shifted backward along the length of the trenches with 10-nm steps, and the milling/imaging process was repeated until the end of the trenches. Therefore, the final product of this process is a stack of 2-D SEM images with a 10-nm spacing between each two successive images for a total of 2000 images per each clay specimen.

Reconstruction of the 3-D tomography

Processing the 2-D images for each of the considered specimens to reconstruct the three-dimensional (3-D) tomography was performed using Avizo Fire 8.1.1 software (Avizo 2016). For each specimen, all images were first aligned to correct for beam drifts and shifts. This image alignment step was twofold; the first step uses an in-house MATLAB code that matches features (e.g., pores and particles) between every two successive images to minimize the overall shifts in the images. The second step then eliminates all remaining drifts using the FIB stack module in Avizo fire and ImageJ (Schneider et al. 2012). It should be noticed that the use of these two alignment steps increased the quality of the final 3-D tomographies compared to using any of these techniques alone.

Once all images for a given specimens were aligned, the quality of each image was enhanced by removing artifacts and strengthening the contrast of the borderlines between the solid clay particles and the pores. These image enhancements were performed by, first, applying a nonlocal means filter that eliminates white noises and artifacts from images as shown in Fig. 3. Then, a nonlinear digital median filter was applied to remove any remaining artifacts while increasing the contrast at solid/pore boundaries as shown in Fig. 3. The 3-D tomography for each specimen

was then reconstructed from the aligned and filtered images using the volume rendering module in Avizo Fire. Figure 4 shows the developed 3-D tomography for the specimen subjected to 70 °C as an example.

To quantitatively estimate the pore size distribution in each specimen, the pores in the developed 3-D tomographies need to be identified; in other words, the developed 3-D tomographies should be segregated to pores and non-pores (i.e., solids) zones. The segregation process was performed using the interactive thresholding module in Avizo Fire, which allows selecting lower and upper thresholds for the grayscale that represents the feature of interest, i.e., the pores in this study. The selected thresholds for all three specimens were the same with a lower threshold of 0 and an upper threshold of 90. Figure 5 shows an example of a segregated 2-D ortho-slice section from the 3-D tomography of the specimen subjected to 70 °C. In this figure, the blue zones represent the pores, while the black zones represent the solid clay particles.

Once the pore structure in each specimen was segregated, the volume of each pore was estimated. The volume estimation of a given pore requires quantifying the number of the digital elements (i.e., voxels) filling the pore and the volume of each voxel. The number of the voxels filling a given pore is provided by the volume rendering module in Avizo Fire. The voxel's volume was determined from the filtered 2-D SEM images by dividing an image dimension (i.e., width or length) by the original image resolution (i.e., voxels along the considered dimension) to estimate the voxel sizes in the image plane. The voxel size in the direction perpendicular to the image plane, i.e., the milling direction along the trenches, is simply the size of the ion beam shift (i.e., 10 nm).

In the end, the pore size (i.e., diameter) distribution for each specimen was calculated from the obtained pore volume distribution for the considered specimen assuming that the clay pores are spherical in nature. It should be noticed that considering spherical pores may not be representative of the actual cylindrical shape of clay pores. However, it is believed that such assumption will cause a systematic error in the same order in the pore size distributions for all specimens; therefore, the use of a comparative study to determine the temperature effects on the pore sizes remains valid.

Results and discussions

The performed quantitative pore size distributions for the three considered clay specimens, presented in Fig. 6a, show that the effective sizes (i.e., diameters) of the pores in the used clay range between 20 and 700 nm (0.7 μm); the maximum pore diameter approximated from the 3-D

Fig. 3 Sequence of applied filters to enhance SEM image quality for 3-D tomography reconstruction

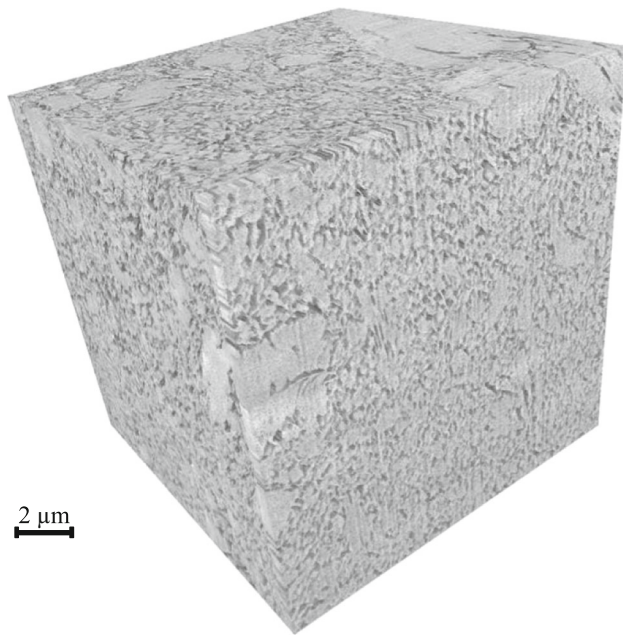
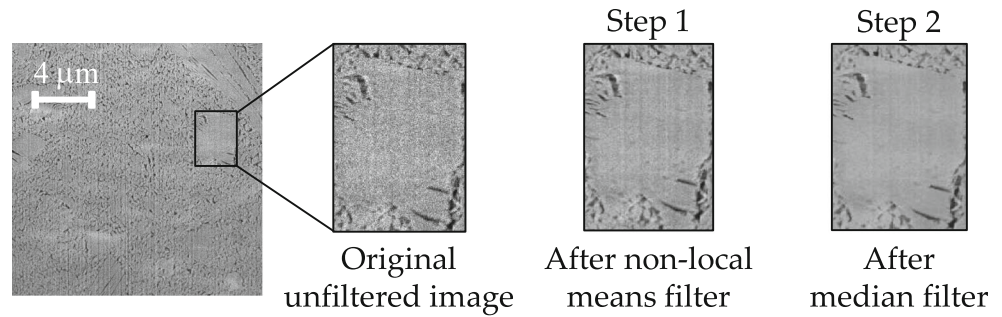


Fig. 4 Reconstructed 3-D tomography for the specimen subjected to 70 °C

tomography agrees with that observed in SEM images as exemplified in Fig. 6b. Furthermore, Fig. 6a shows that smooth pore size distributions exist up to about 200–300 nm beyond which the distributions show slight fluctuations. These fluctuations are due to the limitations of the thresholding techniques to precisely identify the borderlines between the pores and the solids for large pore sizes (Holzer et al. 2004). Such unavoidable thresholding inaccuracy produces a minor systematic error, equal magnitudes, and similar signs, in all approximated pore size distributions, which is believed to be insignificant for the comparative analysis performed in this study. Moreover, since the pore size distribution of the 20 °C specimen shows that about 80% of the pores are smaller than 300 nm, only 20% of the pores for this specimen is expected to be affected by this systematic thresholding error at larger pore sizes.

Compared to the pore size distribution for the specimen at 20 °C, the pore size distribution for the specimen

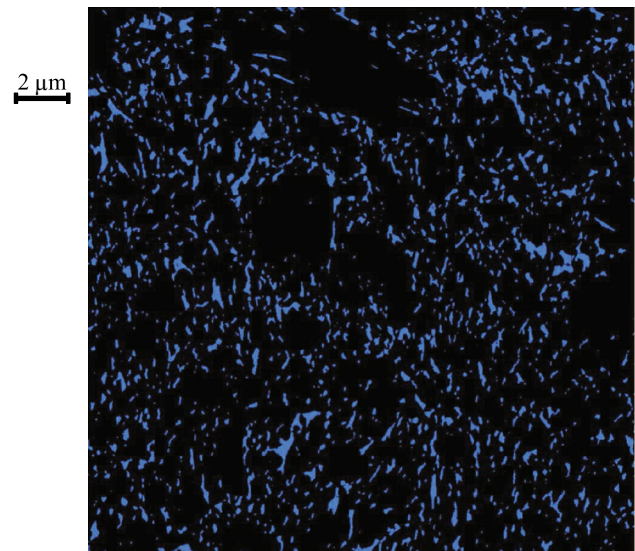


Fig. 5 Segregated 2-D ortho-slice section from the 3-D tomography of the specimen subjected to 70 °C. Blue-colored zones are clay pores, while black-colored zones are solid clay particles

subjected to freezing at $-10\text{ }^{\circ}\text{C}$ is shifted toward larger pore sizes. This shift suggests that freezing increases the sizes of the pores in clays, which can be explained by the thermal expansion of the pore water upon forming ice lenses (Alkire and Morrison 1983; Konrad 1989). It is, also, observed that the freezing-induced increase in the smaller pore sizes (less than about 80 nm) is less than the increase in the sizes of the larger pores, which can be attributed to the higher water volume enclosed in the larger pores compared to that in the smaller pores. Thus, higher volumetric expansions of the water in large pores are expected to occur upon forming ice compared to that in the small pores. However, the increase in the effective pore diameter at all sizes does not correspond to the expected 9% increase in the pore water volume upon forming ice. A 100-nm spherical pore, for example, increased to about 150 nm in diameter upon freezing as shown in Fig. 6a, while it was expected to increase in diameter to 102.9 nm due to the 9% increase in the pore water volume upon forming ice. This may suggest that, in addition to the expected increase in the volume of individual clay pores as

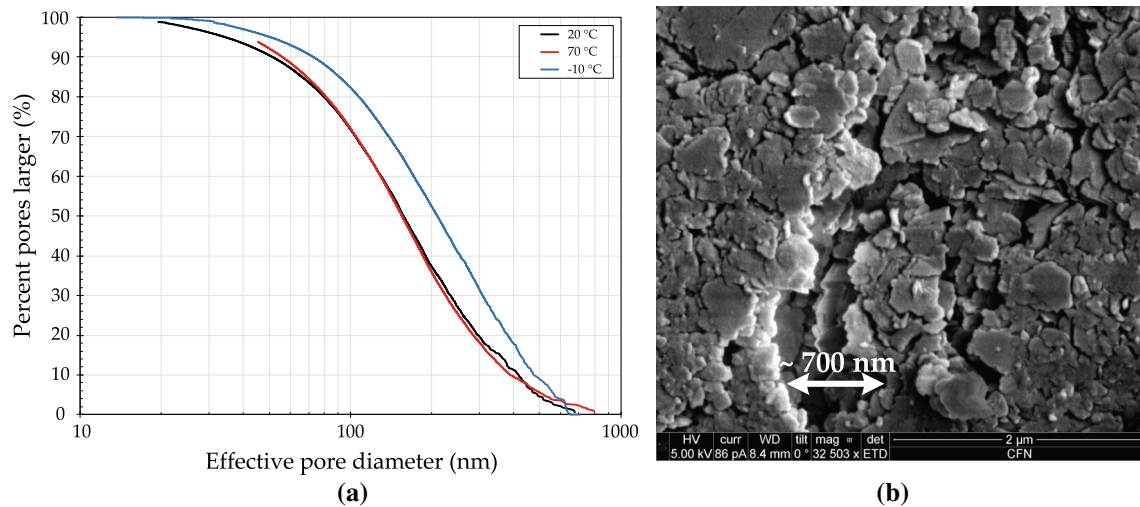


Fig. 6 Results of the analysis: **a** pore size distributions for the specimens subjected to 20, 70, and -10 °C, and **b** a SEM image for the 70 °C specimen confirming the maximum pore size

ice forms, one or both of the following microstructural changes occur upon freezing (1) the original pores merge forming larger pores, and (2) increase in the water content within the pores due to water migration toward the freezing front.

Unlike the observable change in the pore size distribution due to freezing, minor differences are observed between the pore size distribution obtained for the specimen subjected to 70 °C and that obtained for the 20 °C specimen. As shown in Fig. 6a., heating the clay to 70 °C caused a slight increase in the sizes of the small pores, while it decreased in the sizes of the larger pores. The decrease in the size of the larger pores appears to be more than the increase in the size of the small pores since it occurs over a larger range of large pore sizes, which may explain the typically heating-induced contractive volumetric strains observed upon heating clays (Abuel-Naga et al. 2007; Campanella and Mitchell 1968b; Demars and Charles 1982; Sultan et al. 2002; Towhata et al. 1993).

In order to explain the increase in the size of the small pores and the decrease in the size of the large pores upon heating, it is critical to consider the thermally induced volume changes for the pore water and the clay particles as well as the thermally induced pore water flow. This can be explained as follows:

1. It is expected that the heating-induced increase in the pore water volume will require more time to drain out of the small pores compared to the time it takes to drain out of the large pores. Therefore, the pore water in the small pores will have a longer time to expand upon heating compared to larger pores; this, in turn, is expected to increase the volume of the small pores significantly.

2. Despite the relatively fast flow of the heating-induced excess pore water volume out of the large pores, the small decrease in the size of the large pores was not expected. This decrease in the large pore sizes can be explained considering the anisotropic thermal expansion coefficient of clay particles (McKinstry 1965). The thermal expansion coefficients of kaolinite clays in the directions parallel (\parallel) and perpendicular (\perp) to the layers of the clay basic units are (α_{\parallel}) $5 \times 10^{-6} \text{ K}^{-1}$ and (α_{\perp}) $18 \times 10^{-6} \text{ K}^{-1}$, respectively. Therefore, the increase in the thickness of a clay particle upon heating is about 3.6 times more than the increase in the clay surface area, or length. To explain the effects of these anisotropic thermal expansions of clay particles, assume that the initial length and thickness of the clay particles in Fig. 7 are L_0 and t_0 , respectively. Upon heating, all clay particles will expand with the final length and thickness being L_f and t_f , respectively. Thus, the expected increase in the pore area (assuming a unit length into the page) due to particles elongation, ΔA_{p1} , is provided by Eq. (1).

$$\Delta A_{p1} = A_f - A_0 \quad (1)$$

where A_0 and A_f are the initial and the final pore areas, respectively, which can be approximated using the areas enclosed by the four clay particles in Fig. 7 as provided in Eq. (2) and Eq. (3), respectively.

$$A_0 = L_0^2 \quad (2)$$

$$A_f = L_0 \cdot (L_0 + \Delta T \cdot \alpha_{\parallel} \cdot L_0) = L_0^2 + \Delta T \cdot \alpha_{\parallel} \cdot L_0^2 \quad (3)$$

Therefore,

$$\Delta A_{p1} = \Delta T \cdot \alpha_{\parallel} \cdot L_0^2 \quad (4)$$

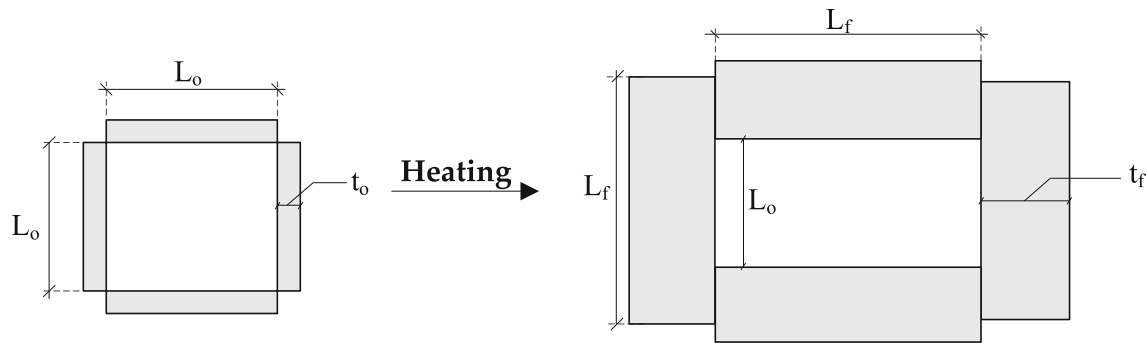


Fig. 7 Schematic showing the effect of the anisotropic thermal expansion coefficient of the clay pore size

However, the increase in the particle thickness causes a decrease in the pore area (ΔA_{p2}). This decrease in the pore area occurs over the full length of all particles with half the increase in thickness, which can be expressed as given in Eq. (5).

$$\Delta A_{p2} = -2 \cdot \alpha_{\perp} \cdot \Delta T \cdot t_o \cdot (L_o + \Delta T \cdot \alpha_{\parallel} \cdot L_o) \tag{5}$$

which can be simplified by ignoring the higher-order term, i.e., the term that includes $\alpha_{\perp} \cdot \alpha_{\parallel}$, as given in Eq. (6).

$$\Delta A_{p2} = -2 \cdot \alpha_{\perp} \cdot \Delta T \cdot t_o \cdot L_o \tag{6}$$

Therefore, the total thermally induced change in the pore area can be approximated as shown in Eq. (7), which subtracts the area decrease due to the thermal expansion of the particles in the lateral direction (ΔA_{p2}) from the area increase due to particles elongation (ΔA_{p1}).

$$\Delta A_t = \Delta T \cdot \alpha_{\parallel} \cdot L_o^2 - 2 \cdot \alpha_{\perp} \cdot \Delta T \cdot t_o \cdot L_o \tag{7}$$

Considering a typical kaolinite particle size of 0.5 μm (about D_{50} for the considered clay) and a thickness of 0.072 μm assuming 100 basic units (Holtz et al. 2011), and assuming a unit temperature change, the total change in the pore volume can be estimated as shown in Eq. (8).

$$\begin{aligned} \Delta A_t &= 5 \times 10^{-6} \cdot (0.5)^2 - 2 \times 18 \times 10^{-6} \times 0.072 \times 0.5 \\ &= -0.046 \times 10^{-6} \text{ K}^{-1} \end{aligned} \tag{8}$$

Equation (8) suggests that the pore area will decrease due to heating justifying the observed decrease in the size of the large pores as shown in Fig. 6. This also justifies the heating-induced contraction observed in clays during drained heating (Abuel-Naga et al. 2007; Campanella and Mitchell 1968b; Cekerevac and Laloui 2004; Demars and Charles 1982; Donna and Laloui 2015; Sultan et al. 2002; Towhata et al. 1993).

Conclusion

This study utilized stacks of 2-D SEM images taken using the SEM/FIB technology to quantify the effects of temperature on the pore size distribution of a kaolinite clay. Three specimens, prepared at different temperatures 20, 70, and -10 $^{\circ}\text{C}$, were used in the analysis. The 2-D SEM images for each specimen were used to reconstruct the 3-D tomography that is quantitatively analyzed to determine the pore size distribution. The results of this study show that freezing clays increases the pore sizes due to the ice formation inside the pores. Further, the increase in the size of the larger pores was found to be more than the increase in the size of the small pores upon freezing because of the larger water volume in the former. On the other hand, the smaller pores increase in size upon heating, while the size of the larger pores decreases. This behavior was explained due to the anisotropic thermal expansion coefficient of clay particles.

Acknowledgment This material is based upon work supported by the US Army Research Laboratory and the US Army Research Office under Contract Number W911NF-16-1-0336. Additionally, this research used resources of the Center for Functional Nanomaterials, which is a US DOE Office of Science Facility, at Brookhaven National Laboratory under Contract No. DE-SC0012704. The discussions and conclusions presented in this work reflect the opinions of the authors only.

References

Abdelaziz S, Ozudogru TY (2016) Selection of the design temperature change for energy piles. *Appl Therm Eng* 107:1036–1045

Abuel-Naga HM, Bergado DT, Soralump S, Rujivipat P (2005) Thermal consolidation of soft Bangkok clay. *Int J Lowl Technol* 17:1–9

Abuel-Naga HM, Bergado DT, Boulazza A (2007) Thermally induced volume change and excess pore water pressure of soft Bangkok clay. *Eng Geol* 89:144–154

Alkire BD, Morrison JM (1983) Change in soil structure due to freeze-thaw and repeated loading. *Transp Res Rec* 918:15–22

Avizo (2016) Avizo user’s guide, 9.0 edn. FEI, Belin (ZIB), Germany

- Baldi G, Hueckel T, Pellegreni R (1988) Thermal volume changes of the mineral-water system in low-porosity clay soils. *Can Geotech J* 24:807–825
- Broms BB, Yao LYC (1964) Shear strength of a soil after freezing and thawing. *J Soil Mech Found Div* 90:1–25
- Burghignoli A, Desideri A, Miliziano S (2000) A laboratory study on the thermomechanical behaviour of clayey soils. *Can Geotech J* 37:764–780
- Campanella RG (1965) Effect of temperature and stress on the time-deformation behavior of saturated clay. University of California, Berkeley
- Campanella RG, Mitchell JK (1968a) Influence of temperature variations on soil behavior. *J Soil Mech Found Div* 94:709–734
- Campanella RG, Mitchell JK (1968b) Influence of temperature variations on soil behavior. *J Soil Mech Found Eng Div* 94:709–734
- Cekerevac C, Laloui L (2004) Experimental study of thermal effects on the mechanical behaviour of a clay. *Int J Numer Anal Meth Geomech* 28:209–228
- Chamberlain EJ (1981) Overconsolidation effects of ground freezing. *Eng Geol* 18:97–110
- Chamberlain EJ, Gow AJ (1979) Effect of freezing and thawing on the permeability and structure of soils. *Eng Geol* 13:73–92
- Coccia CJR, McCartney JS (2016a) Thermal volume change of poorly draining soils I: critical assessment of volume change mechanisms. *Comput Geotech* 80:26–40
- Coccia CJR, McCartney JS (2016b) Thermal volume change of poorly draining soils II: model development and experimental validation. *Comput Geotech* 80:16–25
- Czurda KA, Hohmann M (1997) Freezing effect on shear strength of clayey soils. *Appl Clay Sci* 12:165–187
- Demars KR, Charles RD (1982) Soil volume changes induced by temperature cycling. *Can Geotech J* 19:188–194
- Donna A, Laloui L (2015) Response of soil subjected to thermal cyclic loading: experimental and constitutive study. *Eng Geol* 190:65–76
- Eigenbrod KD (1996) Effects of cyclic freezing and thawing on volume changes and permeabilities of soft fine-grained soils. *Can Geotech J* 33:529–537
- Eriksson LG (1989). Temperature effects on consolidation properties of sulphide clays. Paper presented at the twelfth international conference on soil mechanics and foundation engineering. Rio de Janeiro
- Garham J, Au VCS (1985) Effects of freeze-thaw and softening on a natural clay at low stresses. *Can Geotech J* 22:69–78
- Holtz RD, Kovacs WD, Sheahan TC (2011) An introduction to geotechnical engineering, 2nd edn. Pearson Education, Inc., Upper Saddle River, NJ, USA
- Holzer L, Indutnyi F, Gasser P, Münch B, Wegmann M (2004) Three-dimensional analysis of porous BaTiO₃ ceramics using FIB nanotomography. *J Microsc* 216:84–95
- Hueckel T, Baldi G (1990) Thermoplasticity of saturated clays: experimental constitutive study. *J Geotech Eng* 116:1778–1796
- Hueckel T, François B, Laloui L (2009) Explaining thermal failure in saturated clays. *Géotechnique* 59:197–212
- Knellwolf C, Peron H, Laloui L (2011) Geotechnical analysis of heat exchanger piles. *J Geotech Geoenviron* 137:890–902
- Konrad JM (1987) Procedure for determining the segregation potential of freezing soils. *Geotech Test J* 10:51–58
- Konrad JM (1989) Physical processes during freeze-thaw cycles in clayey silts. *Cold Reg Sci Technol* 16:291–303
- Kuntiwattanakul P, Towhata I, Ohishi K, Seko I (1995) Temperature effects on undrained shear characteristics of clay. *Soils Found* 35:147–162
- Laloui L (2001) Thermo-mechanical behaviour of soils. *Revue Française de Génie Civil* 5:809–843
- Laloui L, Nuth M, Vulliet L (2006) Experimental and numerical investigations of the behaviour of a heat exchanger pile. *Int J Numer Anal Meth Geomech* 30:763–781
- McKinstry HA (1965) Thermal expansion of clay minerals. *Am Mineral* 50:212–222
- Mitchell JK (1969) Temperature effects on the engineering properties and behavior of soils. Highway Research Board, Washington
- Mitchell JK, Soga K (2005) Fundamentals of soil behavior, 3rd edn. London, Wiley
- Norrish K, Rausell-Colom JA (1962) Effect of freezing on the swelling of clay minerals. *Clay Miner Bull* 5:9–16
- Othman MA, Benson CH (1993) Effect of freeze-thaw on the hydraulic conductivity and morphology of compacted clay. *Can Geotech J* 30:236–246
- Paaswell RE (1967) Temperature effects on clay soil consolidation. *J Soil Mech Found Div* 93:9–22
- Plum RL, Esrig MI (1969) Some temperature effects on soil compressibility and pore water pressure. Highway Research Board, Washington
- Qi J, Vermeer PA, Cheng G (2006) A review of the influence of freeze-thaw cycles on soil geotechnical properties. *Permafrost Periglacial Process* 17:245–252
- Qi J, Ma W, Song C (2008) Influence of freeze-thaw on engineering properties of a silty soil. *Cold Reg Sci Technol* 53:397–404
- Qi J, Hu W, Ma W (2010) Experimental study of a pseudo-preconsolidation pressure in frozen soils. *Cold Reg Sci Technol* 60:230–233
- Rowe RK (2012) Short- and long-term leakage through composite liners. The 7th Arthur Casagrande Lecture. *Can Geotech J* 49:141–169
- Schneider CA, Rasband WS, Eliceiri KW (2012) NIH Image to ImageJ: 25 years of image analysis. *Nat Methods* 9:671–675
- Sultan N, Delage P, Cui YJ (2002) Temperature effects on the volume change behaviour of Boom clay. *Eng Geol* 64:135–145
- Tanaka N, Graham J, Crilly T (1997) Stress-strain behaviour of reconstituted illitic clay at different temperatures. *Eng Geol* 47:339–350
- Tang Y, Yan J (2015) Effect of freeze-thaw on hydraulic conductivity and microstructure of soft soil in Shanghai area. *Environ Earth Sci* 73:7679–7690
- Towhata I, Kuntiwattanakul P, Seko I, Ohishi K (1993) Volume change of clays induced by heating as observed in consolidation tests. *Soils Found* 33:170–183
- Wang D-Y, Ma W, Niu Y-H, Chang X-X, Wen Z (2007) Effects of cyclic freezing and thawing on mechanical properties of Qinghai-Tibet clay. *Cold Reg Sci Technol* 48:34–43